ACCEPTED FOR PUBLICATION IN THE ASTROPHYSICAL JOURNAL
Preprint typeset using LaTeX style emulateapj v. 05/12/14

THE LUMINOUS X-RAY HALOS OF TWO COMPACT ELLIPTICAL GALAXIES

DAVID A. BUOTE AND AARON J. BARTH
Department of Physics and Astronomy, University of California at Irvine, 4129 Frederick Reines Hall, Irvine, CA 92697-4575;
buote@uci.edu

Accepted for Publication in The Astrophysical Journal

ABSTRACT

There is mounting evidence that compact elliptical galaxies (CEGs) are "massive relic galaxies" that are local analogs of the high-redshift "red nuggets" thought to represent progenitors of today's early-type galaxies (ETGs). We report the discovery of extended X-ray emission from a hot interstellar / intragroup medium in two CEGs, Mrk 1216 and PGC 032873, using shallow archival *Chandra* observations. We find that PGC 032873 has an average gas temperature $k_BT = 0.67 \pm 0.06$ keV within a radius of 15 kpc of the galaxy, and a luminosity $L_x = (1.8 \pm 0.2) \times 10^{41}$ erg s^{-1} within a projected radius of 100 kpc, the latter of which is estimated by extrapolating the fitted β model to the surface brightness. For Mrk 1216, which is closer and more luminous [$L_x(< 100$ kpc) $= (12.1 \pm 1.9) \times 10^{41}$ erg s^{-1}], the data are of sufficient quality to perform a spatially resolved spectral analysis in seven circular annuli out to a radius of 73 kpc. Using an entropy-based hydrostatic equilibrium procedure, we obtain good constraints on the H-band stellar mass-to-light ratio, $M_{\rm stars}/L_H = 1.33 \pm 0.21$ solar, in good agreement with that obtained from stellar dynamical studies, which supports the hydrostatic equilibrium approximation for this galaxy. We obtain a mass-weighted density slope 2.22 ± 0.08 within R_e consistent with other CEGs and normal local ETGs, while we find the dark matter (DM) fraction within R_e $f_{\rm DM} = 0.20 \pm 0.07$ to be similar to local ETGs. We place a constraint on the SMBH mass, $M_{\rm BH} = (5 \pm 4) \times 10^9 M_\odot$, with a 90% upper limit of $M_{\rm BH} = 1.4 \times 10^{10} M_\odot$, consistent with a recent stellar dynamical measurement. If we assume the Navarro-Frenk-White (NFW) DM scale radius does not lie beyond the current extent of the data, we also obtain interesting constraints on the halo concentration ($c_{200} = 17.5 \pm 6.7$) and mass [$M_{200} = (9.6 \pm 3.7) \times 10^{12} M_\odot$]. The measured c_{200} exceeds the mean ΛCDM value (≈ 7), consistent with a system that formed earlier than the general halo population. We suggest that these galaxies, which reside in group-scale halos, should be classified as fossil groups.

1. INTRODUCTION

Over the past decade it has become increasingly clear that most early-type galaxies (ETGs) form and evolve via a two-stage process (e.g., Oser et al. 2010). Initially, the galaxy collapses and rapidly evolves through strong dissipation and wet mergers assembling most of its stellar mass and becoming a "red nugget" by $z \approx 2$. Compared to the present-day ETG population, red nuggets are much more compact and have disky isophotes consistent with being fast rotators. The second phase of ETG evolution is a gradual build-up of its stellar envelope around the core red nugget through mostly dry mergers and passive evolution of its stellar population. This is reflected in the well-established size-mass evolution of ETGs (e.g., van Dokkum et al. 2008) and through multi-component decompositions of nearby ETGs (Huang et al. 2013). Unfortunately, because red nuggets exist at high redshift it has not been possible yet to measure radial mass profiles in detail to probe more effectively the first phase.

A new way to approach studying red nuggets in more detail is through local analogs. There is mounting evidence that compact elliptical galaxies (CEGs; e.g., van den Bosch et al. 2015) are indeed largely untouched, passively evolved descendants of the high-redshift red nuggets. The CEGs possess many of the same basic properties (e.g., small size, large stellar mass, etc.), but only a relatively small number of CEGs have been studied in detail. In the largest and most comprehensive study to date, Yıldırım et al. (2017, hereafter Y17) present stellar dynamical models of IFU kinematic data along with stellar populations studies of 16 CEGs. Three of these have also been studied recently by Ferré-Mateu et al. (2017) in detail confirming their identification as "massive relic galaxies" (MRGs). Yıldırım et al. (2017) find that within $1R_e$ both the total mass slope and the mean stellar mass fraction are higher than present-day ETGs. They argue that both of these properties are consistent with dissipative formation for the red nuggets. Y17 also argue their analysis of the CEGs disfavors adiabatic contraction of their DM halos, which would represent an important constraint on the ubiquity of that evolutionary process (e.g., Blumenthal et al. 1986; Gnedin et al. 2004; Dutton et al. 2015).

Finally, CEGs/MRGs have generated significant interest since several studies suggest that they possess super-massive black holes (SMBHs) that are positive outliers (i.e., übermassive) at the high-mass end ($> 10^9 M_\odot$) of the BH-mass scaling relations (e.g., Ferré-Mateu et al. 2015; van den Bosch et al. 2015; Walsh et al. 2015; Yıldırım et al. 2016; Walsh et al. 2017), similar to those BHs found in some BCGs (e.g. McConnell et al. 2012; Rusli et al. 2013; Thomas et al. 2016).

What has been learned so far for the mass profiles has been achieved only through stellar dynamics. These systems are too nearby for studies with gravitational lensing. However, they are potentially ideal sites for hydrostatic equilibrium (HE) studies of their hot gas, given that they are believed to be largely untouched, passively evolved descendants of the high-redshift universe. HE allows the gravitating mass to be derived directly from the temperature and density profiles of the ISM, from the center to the halo outskirts using a single dynamical tracer.

In this paper we describe a search for promising CEG/MRG targets to apply the HE approach to study the mass profiles to complement and augment what has and is currently being

learned from stellar dynamics. In §2 we identify the CEG sample in which we searched for targets with extended X-ray emission suitable for HE analysis from which we identify two promising galaxies, Mrk 1216[1] and PGC 032873. We describe the *Chandra* X-ray observations and data preparation in §3. We define the models used for spectral analysis in §4. In §5 we present results for PGC 032873. For Mrk 1216 we describe the models and results in §6. We present an analysis of the image properties in §6.1, and the results of the spectral analysis in §6.2. The HE models are presented in §6.3 and the results in §6.4. We present our conclusions in §7.

2. CEG SAMPLE

We searched for promising CEG targets for HE study of their hot ISM using the new catalog of Y17 which presents stellar dynamical studies of 16 nearby CEG. We summarize the results of our initial survey of X-ray data archives as follows.

- No *Chandra* or *XMM-Newton* data – NGC 384, NGC 472, NGC 2767, PGC 70520
- Nuclear point sources with little extended emission – UGC 2698 and UGC 3816
- ULX (Walton et al. 2011) with little extended emission – NGC 3990
- Negligible / Insufficient diffuse emission – PGC 011179, PGC 12562, NGC 1282
- Perseus cluster galaxies for which determining the extended nature of emission is problematical due to the source being far off-axis, on a chip edge, and/or swamped by intracluster medium – NGC 1270, NGC 1271, NGC 1277, NGC 1281
- Isolated galaxies with luminous, extended X-ray emission – Mrk 1216 and PGC 032873

Unfortunately, most of the CEGs in the Y17 catalog are not promising for study presently for a variety of reasons. Some lack any *Chandra* or *XMM-Newton* data to search for extended emission. Most of the targets do not show clear evidence for substantial extended emission with the existing data. However, two targets are very promising for HE study of extended X-ray emission: (1) Mrk 1216 and (2) PGC 032873. Both of these objects are recently very well-studied in optical/IR confirming their status as MRGs (Ferré-Mateu et al. 2017; Yıldırım et al. 2017) and possibly with over-massive SMBHs (e.g., Ferré-Mateu et al. 2015; Walsh et al. 2017). We list their basic properties in Table 1 and below analyze in detail their extended X-ray emission.

3. OBSERVATIONS AND DATA PREPARATION

In Table 2 we list details of the *Chandra* observations of Mrk 1216 and PGC 032873. Unless stated otherwise, the data were prepared as described in Buote (2017, hererafter B17), and we refer the reader to that paper for details. We used the *CIAO* (v4.9) and *HEASOFT* (v6.18) software suites along with version 4.7.5.1 of the *Chandra* calibration database to prepare the data for imaging and spatially resolved spectral analysis. For the imaging analysis, we extracted images from the cleaned events lists with energies $0.5-7.0$ keV and employed 1.7 keV monochromatic exposure maps.

For the spectral analysis, we required a minimum 200 source counts for each concentric circular annulus. In the case of PGC 032873, this resulted in only a single aperture ($R = 30'' = 15.1$ kpc). We also included a larger annulus ($R = 30''-150''$) to help constrain the background. For Mrk 1216 our criterion resulted in seven annuli (see Table 3) extending out to 73 kpc (2.′7) plus a larger annulus (2.′7-4.′1) for aiding background constraints.

We also examined the likelihood that enhanced Solar Wind Charge Exchange (SWCX) emission significantly impacted the observations. We obtained the solar proton flux during each *Chandra* observation using the Level 3 data from SWEPAM/SWICS[2]. Both observations have solar proton flux below $\approx 2\times10^8$ cm^{-2} s^{-1} indicating significant proton flare contamination is not expected (Fujimoto et al. 2007).

4. SPECTRAL MODELS

We performed frequentist fits of the plasma and background emission models to the spectra using XSPEC v12.9.0s (Arnaud 1996). We chose to minimize the C-statistic (Cash 1979) since it is largely unbiased compared to χ^2 (e.g. Humphrey et al. 2009b). We modeled the hot ISM with the VAPEC plasma emission model and the cosmic and particle backgrounds with a combination of power-laws and gaussians. For both galaxies the unresolved LMXB contribution is unimportant, and we modeled it as a 7.3 keV thermal bremsstrahlung component (e.g., Matsumoto et al. 1997; Irwin et al. 2003) with normalization fixed by the $L_x - L_K$ scaling relation for unresolved discrete sources of Humphrey & Buote (2008) using the K-band luminosity listed in Table 1. The hot ISM components are allowed to vary between the annuli while the background components are tied. For each galaxy, the background models are also fitted in the extra large annulus (§3), which provides the key constraints on the background. We refer the reader to §3 of B17 for details of the models and fitting procedure.

For Mrk 1216 we found the soft Cosmic X-ray Background (CXB) components fitted to negligible fluxes with large errors. Consequently, for that galaxy we fixed the soft CXB normalizations to those obtained from fitting *ROSAT* data using the HEASARC X-ray Background Tool[3].

5. PGC 032873

In Figure 1 we display the image overlaid with contours for the central region ($\approx 15''$) of PGC 032873. Although the number of source counts is small (only ≈ 170 within the displayed circle), extended emission centered on the stellar light is clearly observed. The morphology of the X-ray isophotes is broadly consistent with that of the H-band image reported by Y17; i.e., isophotal ellipticity 0.53 and position angle 42°. (In Figure 1 North is up and East is to the left.)

We also plot in Figure 1 the spectrum and best-fitting model in a circular aperture with radius $R = 30'' = 15.1$ kpc containing ≈ 200 source counts. The temperature of the hot ISM within the aperture is well constrained, $k_BT = 0.67\pm0.06$ keV

[1] Shortly before this paper was submitted for publication, a paper describing an analysis of gas heating and cooling using the *Chandra* data of Mrk 1216 was submitted to MNRAS and posted to arXiv.org by Werner et al. (2017).

[2] http://www.srl.caltech.edu/ACE/ASC/level2/sweswi_l3desc.html

[3] https://heasarc.gsfc.nasa.gov/cgi-bin/Tools/xraybg/xraybg.pl

Table 1
Target Properties

Name	Redshift	Distance (Mpc)	Scale (kpc/arcsec)	$N_{\rm H}$ (10^{20} cm^{-2})	$L_{\rm IR}$ ($10^{11}\,L_{\odot}$)	R_e (kpc)	σ_e (km/s)	$L_{\rm x}$ (10^{41} ergs s^{-1})	$k_{\rm B}T$ (keV)
Mrk 1216	0.021328	97.0	0.45	4.0	1.14	2.3	308	12.1 ± 1.9	0.76 ± 0.02
PGC 032873	0.024921	108.8	0.50	1.2	1.21	1.7	304	1.8 ± 0.2	0.67 ± 0.06

Note. — The redshift is taken from NED[a]. We compute the distance in our assumed cosmology using the redshift (also taken from NED) corrected to the reference frame defined by the 3K background. We calculate the Galactic column density using the HEASARC W3NH tool based on the data of Kalberla et al. (2005). The total IR luminosities and circularized effective radii (R_e) are taken from Y17 for Mrk 1216 (H-band) and from 2MASS for PGC 032873 (K-band). The stellar velocity dispersions within R_e are taken from Y17 for both systems. $L_{\rm x}$ is the bolometric (0.1-50.0 keV) luminosity computed using the best-fitting hydrostatic model for each galaxy within an extrapolated projected radius 100 kpc (§6.4). The temperatures are average values computed within 73 kpc for Mrk 1216 (§6.2) and 14.1 kpc for PGC 032873 (§5).

[a]http://ned.ipac.caltech.edu

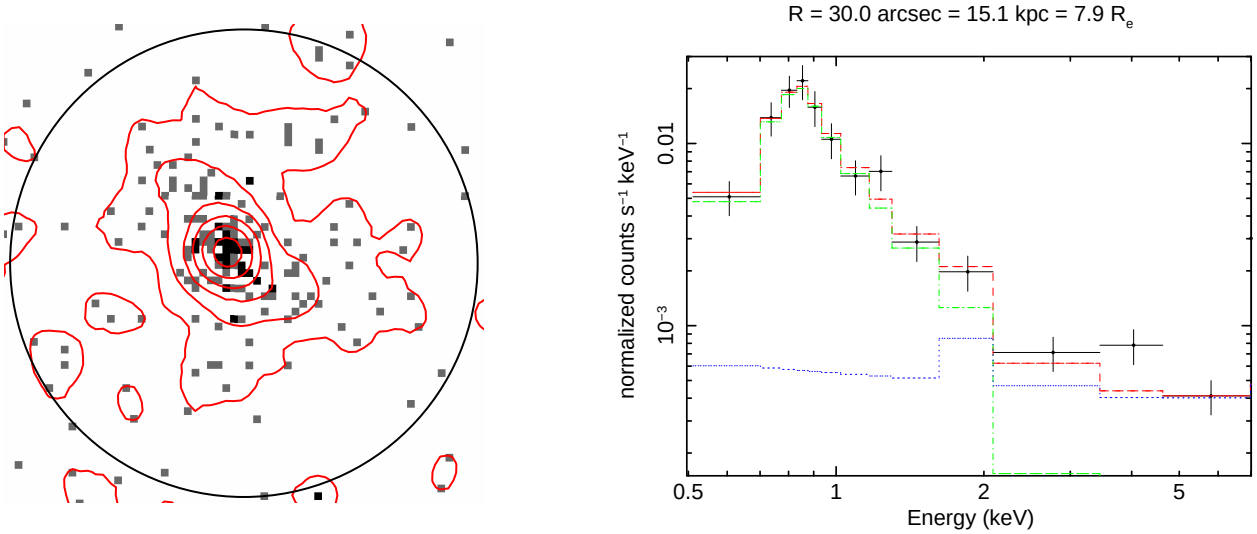

Figure 1. Image and spectrum of PGC 032873. (*Left Panel*) *Chandra* image (0.5-7.0 keV, 0.″492 pixels) with contours overlaid with square-root spacing. Also shown is a circle of radius 15″ = 7.5 kpc for scale. Note this is the raw image used only for display purposes; i.e., no exposure correction or background-subtraction has been applied. (*Right Panel*) *Chandra* spectrum extracted within a radius of 30″. The best-fitting spectral model is shown: hot gas + unresolved discrete sources (LMXBs) + CXB (green), particle background (blue), total model (red).

Table 2
Observations

Galaxy	Obs. ID	Obs. Date	Instrument	Exposure (ks)
Mrk 1216	17061	2015 Jun. 12	ACIS-S	12.8
PGC 032873	17063	2015 Mar. 2	ACIS-S	22.7

Note. — The exposure times refer to those obtained after filtering the light curves, which for each galaxy resulted in < 1 ks of excluded time.

with a sub-solar (though less certain) metallicity, $Z = 0.42 \pm 0.23 Z_{\odot}$. The best-fitting aperture luminosity is $L_{\rm x} = 6.8 \times 10^{40}$ erg s^{-1} (0.5-7.0 keV). These properties are indicative of a typical X-ray luminous massive elliptical galaxy (e.g., Humphrey et al. 2006); e.g., using the mass-temperature scaling relation of galaxy groups from Lovisari et al. (2015) gives $M_{500} = 2 \times 10^{13}\,M_{\odot}$.

Since the data are insufficient for spectral analysis in multiple apertures, we also estimate the radial mass profile using the surface brightness profile and approximating the gas as isothermal. In Figure 2 we show the 0.5-7.0 keV radial surface brightness profile out to a radius of 3′. We fitted a model to the surface brightness consisting of (1) an isothermal β model (Cavaliere & Fusco-Femiano 1978) for the hot gas; (2) a de Vaucouleurs model following the K band light (Table 1) normalized as described in §4 to represent the unresolved LMXB component; and (3) two constant background components, one of which represents the particle background and is not corrected by the exposure map.

The composite model is a good fit to the surface brightness profile and yields for the β model a core radius $0.''6 \pm 0.''3$, slope parameter $\beta = 0.50^{+0.03}_{-0.02}$, and best-fit central density, $\rho_{\rm gas,0} = 9.5 \times 10^{-25}$ g cm^{-3}. Assuming HE and using these best-fitting parameters along with the temperature and metallicity obtained for the spectrum quoted above, the best-fit β model profile yields a total mass, $M_{500} = 1.3 \times 10^{13}\,M_{\odot}$, very consistent with the value obtained above from a scaling relation when considering the large statistical uncertainties.

6. MRK 1216

6.1. *Image Properties*

We show the 0.5-7.0 keV *Chandra* image of the central $\sim 15''$ of Mrk 1216 in Figure 3 with contours overlaid. Like PGC 032873, the X-ray image of Mrk 1216 shows its emis-

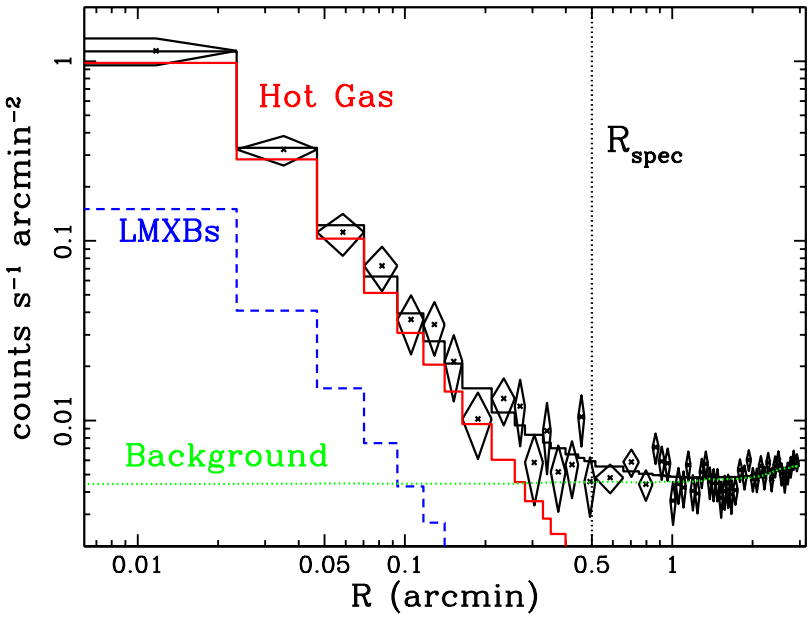

Figure 2. 0.5-7.0 keV radial surface brightness profile and best-fitting model for PGC 032873 (see §5). The vertical dotted line indicates the spectral extraction aperture at radius $R_{\rm spec} = 30'' = 15.1$ kpc.

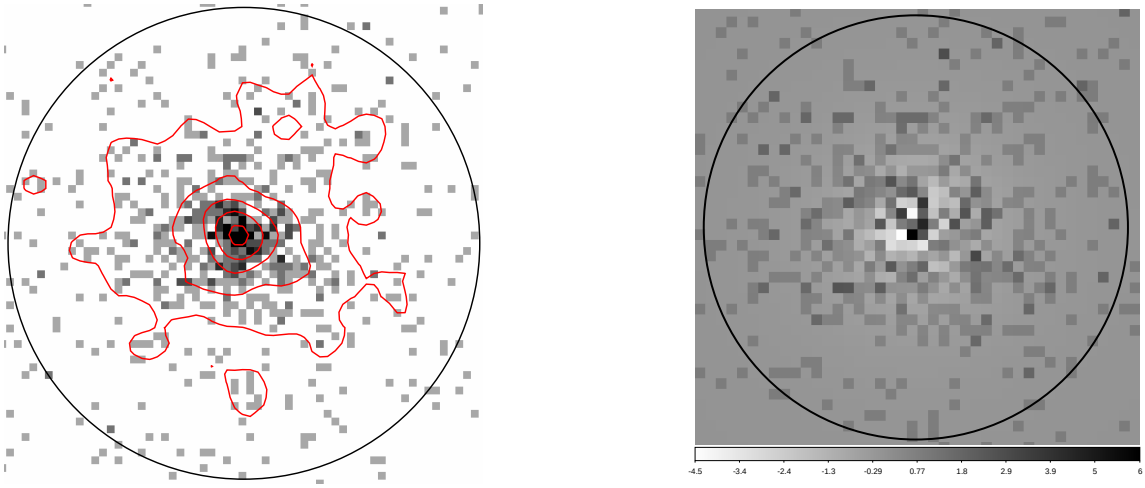

Figure 3. 0.5-7.0 keV *Chandra* image (0.″492 pixels) and residuals for Mrk 1216. (*Left Panel*) Image with contours overlaid with square-root spacing. Also shown is a circle of radius $15'' = 6.7$ kpc for scale. Note this is the raw image used only for display purposes; i.e., no exposure correction or background-subtraction has been applied. (*Right Panel*) Residuals obtained after subtracting the best-fitting circular β-model fitted to the exposure-corrected image. (The displayed circle has a radius of $10''$.) The spatial fluctuations near the galaxy's center are not statistically significant.

sion is clearly extended and is centered on the peak of the stellar light. The displayed region contains ≈ 750 source counts allowing for a more detailed analysis than was possible for PGC 032873. After identifying point sources with the *CIAO* WAVDETECT tool we replaced them with local background using the *CIAO* DMFILTH tool. We then computed the ellipticity and position angle of the surface brightness brightness as a function of semi-major axis using an iterative moment technique equivalent to diagonalizing the moment of inertia tensor (Carter & Metcalfe 1980; see Buote & Canizares 1994 for application to X-ray images of elliptical galaxies).

Within the displayed region the X-ray position angle (PA, measured N through E) is consistent with following the *H*-band stellar light reported by Y17 (70.5°), while the ellipticity is smaller than the *H*-band value ($\epsilon = 0.42$); e.g., for semi-major axis $10''$ we obtain $\epsilon = 0.24 \pm 0.07$ and PA $= 71° \pm 11°$. The rounder X-ray isophotes compared to the stars suggests the X-ray emission follows the gravitational potential obeying approximate HE. This is further supported by the lack of any centroid variation.

To search for image irregularities in more detail, we used the *CIAO* package SHERPA to fit a circular β model to the image and subtract the best-fitting model yielding the residual image shown in the right panel of Figure 3. (Note that for this calculation the image was first corrected with a 1.5 keV monochromatic exposure map. However, we found the results were affected negligibly whether or not the exposure correction was applied.) We do not find any statistically significant features in the residual image. Hence, with the present data, the X-ray emission of Mrk 1216 appears to be very regular and consistent with a relaxed system.

6.2. *Spectral Analysis*

We obtain a good joint fit to the spectra in the seven annuli with a minimum C-statistic of 318 for 289 degrees of freedom (dof). The χ^2 value for this fit is 312 yielding a null hypothesis probability of 17% for a formally acceptable fit. The good quality of the global fit is apparent in Figure 4 where we show the best-fitting model over-plotted on the spectra in two of the annuli.

In Table 3 we list the surface brightness (Σ_x), temperature (k_BT), and the metallicity (Z) for the hot gas component in each annulus. The metallicity parameter is defined such that all the metal abundances other than iron are tied to iron in their solar ratios, where we use the solar abundance table of Asplund et al. (2006). The radial profiles of Σ_x and k_BT are plotted in Figure 5.

The temperature declines from a maximum value of $\approx$ 1 keV in the central radial bin to ≈ 0.6 keV in the outermost aperture very similar to the temperature profile of NGC 6482 (B17). The source emission in the central bin where the temperature peaks is well described by thermal plasma emission. We found no evidence for spectrally hard non-thermal emission in the central bin when adding a power-law component potentially associated with the weak radio source detected in the NVSS (Condon et al. 1998). (Since in §7 we will have use of the average temperature, when tying k_BT for all the apertures we obtain, $k_BT = 0.76 \pm 0.02$ keV.)

The metallicity is consistent with a significant negative radial gradient; i.e., Z declines from $Z \approx 1 Z_\odot$ at the center to $Z \approx 0.4 Z_\odot$ in the outer radial bin similar to NGC 6482 (B17), NGC 5044 (Buote et al. 2003) and other massive elliptical galaxies and small groups (e.g., Buote 2000a; Humphrey & Buote 2006; Mernier et al. 2017). While the data are consistent with the metallicity gradient, it is not required. A fit of similar quality is obtained for a constant $Z = 0.73^{+0.23}_{-0.16} Z_\odot$. The statistical errors on the iron abundance (which dominates the metallicity) are sufficiently large to render unimportant any Fe bias (e.g., Buote 2000b) from fitting a single temperature model to a multi-temperature spectrum (such as that arising from the line-of-sight projection of a radial temperature gradient). We therefore focus our analysis on single-temperature models of the hot ISM in each annulus

We also found that allowing other elements (i.e., O, Ne, Mg, Si, S) to vary separately from Fe resulted in little improvement in the fit and poorly constrained non-Fe abundances. The strongest statement that we can report regarding these is that the ratios Z_{Mg}/Z_{Fe} and Z_{Si}/Z_{Fe} are less than solar at 90% confidence.

6.3. *Hydrostatic Equilibrium Models*

We adopt a bayesian entropy-based procedure to fit spherical HE models of the hot ISM to the *Chandra* spectral data (Humphrey et al. 2008; see Buote & Humphrey 2012a for a review of this and other HE approaches). The biases associated with assuming spherical symmetry are small generally (e.g., Buote & Humphrey 2012b), and they are negligible in our present investigation relative to the large statistical errors on the fitted parameters. We refer the reader to B17 for details of the implementation of the method. Here we briefly summarize the fiducial model components used for Mrk 1216.

- **Entropy** Power-law plus a constant, $S(r) = s_0 + s_1 r^\alpha$, where $S \equiv k_B T n_e^{-2/3}$ is the entropy proxy expressed in units of keV cm^2, r is expressed in kpc, and s_0, s_1, and α are free parameters. We also require at some radius outside the data extent that the logarithmic entropy slope match the value ≈ 1.1 from cosmological simulations with only gravity (e.g., Tozzi & Norman 2001; Voit et al. 2005). We adopt a radius of 100 kpc for this purpose.

- **Pressure** The pressure boundary condition for the solution of the HE equation is a free parameter. We designate this "reference pressure" P_{ref} to be located at a radius 10 kpc.

- **Stellar Mass** Multi-gauss expansion (MGE) model of the *HST* H-band light reported by Y17. This stellar light profile is converted to stellar mass via the stellar mass-to-light ratio (M_{stars}/L_H), which is a free parameter in our model.

- **Dark Matter** NFW profile (Navarro et al. 1997) with free parameters concentration and mass.

- **SMBH** We fix $M_{BH} = 4.9 \times 10^9 M_\odot$ to the stellar dynamical value (Walsh et al. 2017) for the fiducial HE model and discuss results obtained for other M_{BH} values in §6.4.4.

Hence, our fiducial HE model has three free parameters for entropy, one for pressure, one for stellar mass, and two for the DM; i.e., a total of seven free parameters.

6.4. *Results*

6.4.1. *Overview*

We use a bayesian nested sampling procedure based on the MultiNest code v2.18 (Feroz et al. 2009) to fit the HE model to the *Chandra* data (see B17 for details). For the free parameters we use flat priors except for P_{ref} and (M_{DM}) for which we adopt flat priors on their logarithms. The ranges of the priors were chosen to be large enough so that the best-fitting values were far from the boundaries as judged by the standard deviation of the parameter. The one exception to this is the NFW scale radius (r_s) for which the upper limit is poorly constrained. Consequently, we set the maximum value of the prior for r_s to 50 kpc representing essentially the average radius of the outer *Chandra* bin.

We quote two "best" values for each free parameter: "Best Fit", the mean parameter value of the posterior, and "Max Like", the parameter value that maximizes the likelihood. Errors quoted are the standard deviation (1σ) of the posterior unless stated otherwise. In Figure 5 we show the best-fitting fiducial model to the Σ_x and k_BT profiles and the fractional residuals. The fit is excellent as judged by the small fractional residuals. We have also performed a standard frequentist χ^2

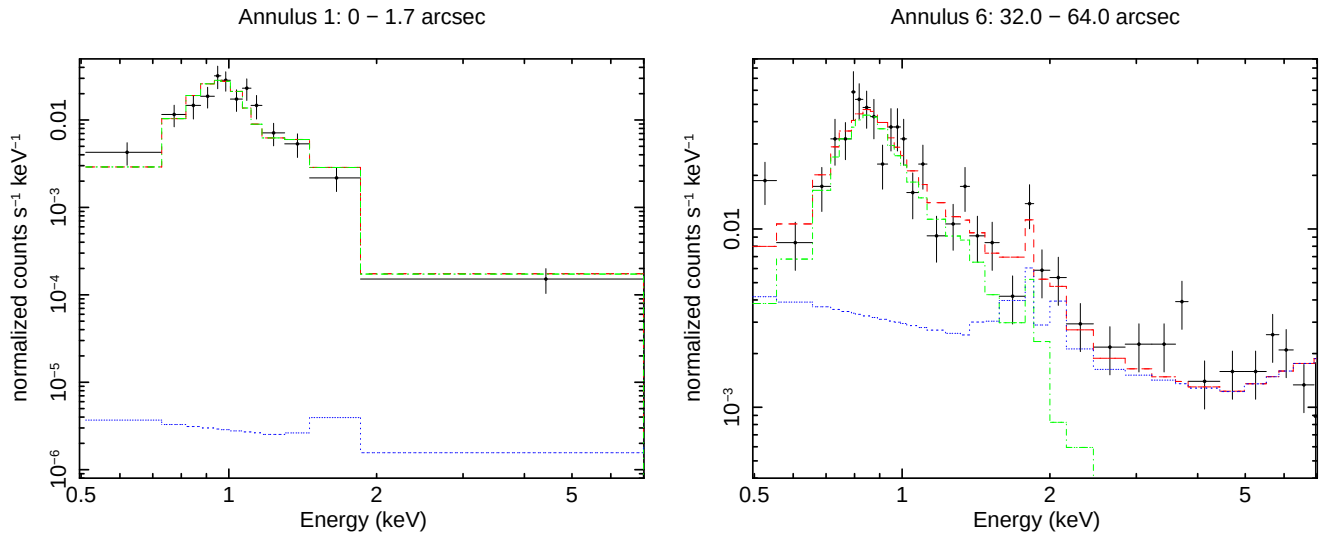

Figure 4. Example *Chandra* spectra for Mrk 1216 in the 0.5-7.0 keV band without any background subtraction. Also plotted are the best-fitting models (red dashed) broken down into the separate contributions from the following: (1) hot gas and unresolved LMXBs from Mrk 1216 along with the CXB (green dot-dash), and (2) particle background (blue dotted).

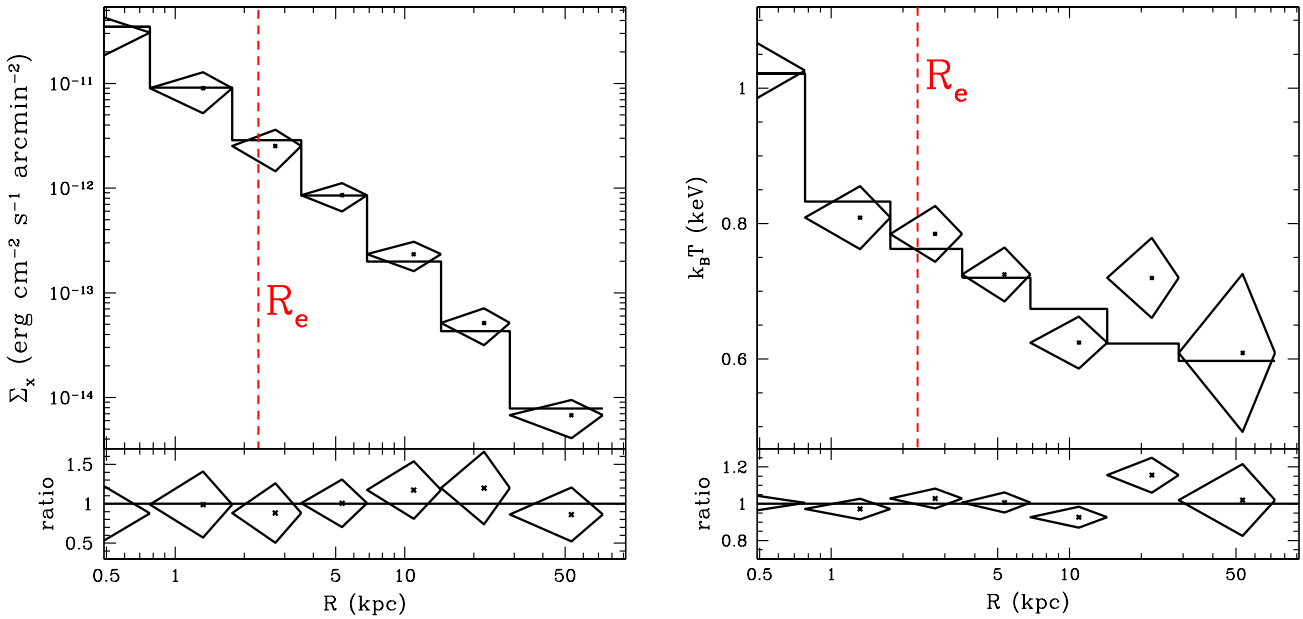

Figure 5. *Chandra* data, 1σ errors, and the best-fitting fiducial hydrostatic model in each circular annulus on the sky for Mrk 1216. (*Left Panel*) Surface brightness (0.5-7.0 keV). See the notes to Table 3 regarding the error bars on Σ_x. (*Right Panel*) Projected emission-weighted temperature (k_BT). Also shown is the location of the stellar half-light radius (R_e). The bottom panels plot the data/model ratios.

analysis to provide another means of judging the goodness-of-fit. This fit yields parameters extremely similar to the "Max Like" parameters of the bayesian fit and $\chi^2 = 5.3$ for 7 degrees of freedom (dof).

Omitting the stellar mass component gives $\chi^2 = 14.2$ for 8 dof; i.e., the *Chandra* data require the stellar mass component at the 99% level according to the F-test. If instead the DM halo is omitted, then $\chi^2 = 65.7$ for 9 dof, showing that the *Chandra* data require it at the $\approx 4\sigma$ level. This X-ray evidence for DM in Mrk 1216 is noteworthy in light of recent stellar dynamical studies that yield conflicting results for the need for a DM halo based on near-IR data; i.e., Y17 do not require DM while Walsh et al. (2017) do require it.

For reference, the best-fit virial radii are: $r_{2500} = 150 \pm 17$ kpc, $r_{500} = 295 \pm 38$ kpc, and $r_{200} = 429 \pm 56$ kpc. The extent of the data is $\approx r_{2500}/2$ which we indicate in Figure 6. Since the outer bin is large, more relevant for the HE models is the average bin radius ≈ 50 kpc or $\approx r_{2500}/3$.

6.4.2. *Entropy*

We plot the entropy profile in Figure 6 with the entropy scaled by $S_{500} = 46.1$ keV cm^2 (see eqn. 3 of Pratt et al. 2010) and give the parameter constraints in Table 4. The entropy profile shape is similar to that of other massive elliptical galaxies (e.g., Humphrey et al. 2008, 2009a, 2011, 2012a; Werner et al. 2013; Buote 2017). Note the slope α is some-

Table 3
Hot Gas Properties for Mrk 1216

Annulus	R_{in} (kpc)	R_{out} (kpc)	Σ_x (0.5-7.0 keV) (ergs cm^2 s^{-1} arcmin^{-2})	k_BT (keV)	Z (solar)
1	0.00	0.78	3.06e-11 $\pm$ 1.21e-11	1.026 ± 0.041	1.04 ± 0.58
2	0.78	1.77	9.00e-12 $\pm$ 3.81e-12	0.809 ± 0.046	tied
3	1.77	3.54	2.52e-12 $\pm$ 1.08e-12	0.785 ± 0.041	tied
4	3.54	6.86	8.55e-13 $\pm$ 2.57e-13	0.725 ± 0.040	0.65 ± 0.34
5	6.86	14.38	2.34e-13 $\pm$ 7.28e-14	0.624 ± 0.038	tied
6	14.38	28.77	5.15e-14 $\pm$ 1.98e-14	0.720 ± 0.059	0.38 ± 0.21
7	28.77	73.03	6.78e-15 $\pm$ 2.68e-15	0.609 ± 0.117	tied

Note. — 1 kpc = 2.22″. Annuli where the metallicity is linked to the value in the previous annulus are indicated as "tied." Note that the definition of Σ_x is essentially the emission measure (i.e., XSPEC NORM parameter, which is the parameter actually fitted to the spectral data) multiplied by the plasma emissivity divided by $\pi\theta^2$ (arcmin^2), where θ is the aperture radius in arcminutes. Rather than quote the results for NORM itself, we have used the best-fitting plasma emissivity for each annulus (i.e., the plasma emissivity evaluated using the best-fitting k_BT and metallicity Z) to convert NORM into a surface brightness unit. Consequently, the error bars quoted for Σ_x are directly proportional to the error bars for NORM.

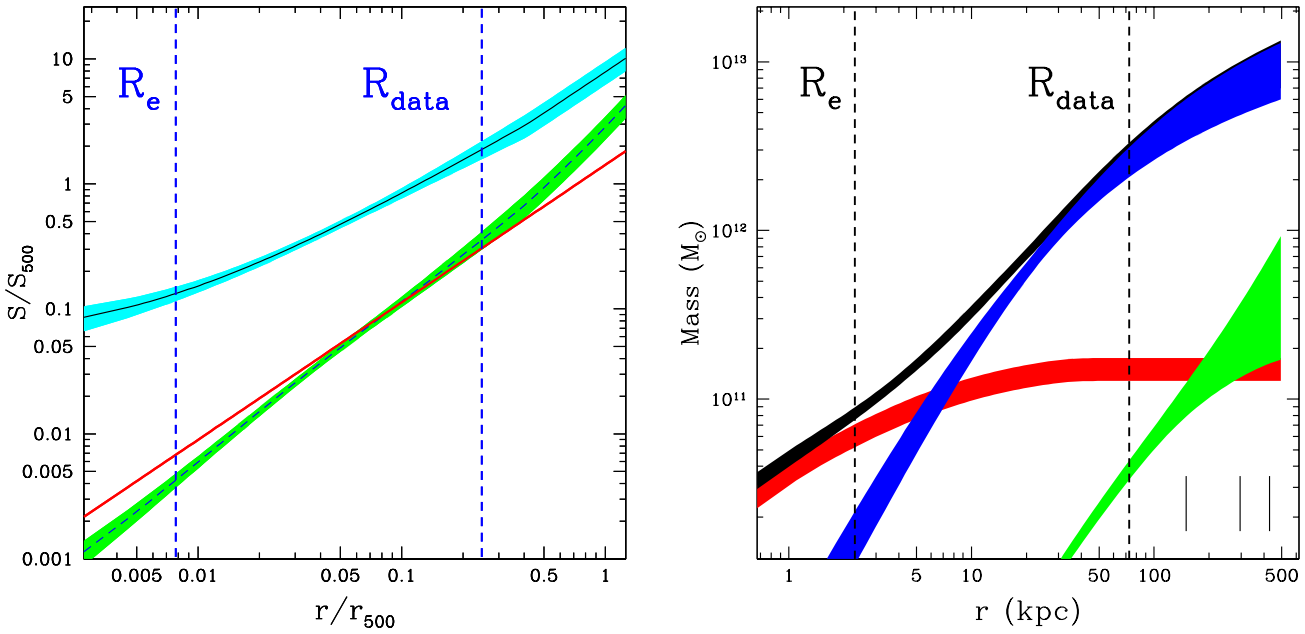

Figure 6. Results for the HE modeling of Mrk 1216. The curved lines and associated shaded regions in both plots show the mean and standard deviation of the posterior as a function of radius for the quantity of interest; i.e., entropy or mass. (*Left Panel*) Radial profile of the entropy (black) and 1σ error region (cyan) for the fiducial hydrostatic model rescaled by $S_{500} = 46.1$ keV cm^2. The baseline $r^{1.1}$ profile obtained by cosmological simulations (Voit et al. 2005) with only gravity is shown as a red line. The result of rescaling the entropy profile by $\propto f_{gas}^{2/3}$ Pratt et al. (2010) is shown by the black dashed line (and green 1σ region). (*Right Panel*) Radial profiles of the total mass (black) and individual mass components of the fiducial hydrostatic model: total NFW DM (blue), stars (red), hot gas (green). The black vertical lines in the bottom right corner indicate the virial radii; i.e., from left to right: r_{2500}, r_{500}, and r_{200}. The vertical dashed lines indicate the location of the stellar half-light radius (R_e) and the outer extent of the *Chandra* data analyzed (R_{data}).

what shallower than the $\sim r^{1.1}$ baseline model, though the difference is only weakly significant ($\approx 1.6\sigma$).

We also show in Figure 6 the baseline gravity-only model. The entropy profile of Mrk 1216 lies well above it testifying to the presence of non-gravitational heating. Rescaling the entropy profile by $(f_{gas}/f_{b,U})^{2/3}$, where f_{gas} is the cumulative gas fraction and $f_{b,U} = 0.155$ is the cosmic baryon fraction, results in much better agreement with the gravity-only model, especially within the region covered by the *Chandra* data. This suggests that the non-gravitational heating has not increased the gas temperature but instead has redistributed the gas spatially. This result is very consistent with those we have obtained previously for the massive isolated elliptical galaxies NGC 720 (Humphrey et al. 2011), NGC 1521 (Humphrey et al. 2012b), and NGC 6482 (B17) and results for galaxy clusters (e.g., Pratt et al. 2010).

We mention that we investigated adding a break radius to the entropy (see equation 3 of B17) and found the data did not require it. Including such a break yielded an entropy profile and overall HE solution very consistent with the no-break case.

6.4.3. *DM Profile*

While the DM halo is clearly required (§6.4.1), the data do not distinguish between profiles with central cusps (NFW, Einasto) and cores (logarithmic potential $\ln(r_c^2 + r^2)$). More-

Table 4
Results for HE Mass Model of Mrk 1216

	$P_{\rm ref}$ (10^{-2} keV cm^{-2})	s_0 (keV cm^2)	s_1 (keV cm^2)	α	$M_\star/L_H$ ($M_\odot L_\odot^{-1}$)	c_{200}	M_{200} ($10^{12}\,M_\odot$)	$f_{\rm gas,200}$	$f_{\rm b,200}$
Best Fit	0.98 ± 0.10	2.49 ± 1.19	2.07 ± 0.71	0.92 ± 0.11	1.33 ± 0.21	17.5 ± 6.7	9.6 ± 3.7	0.051 ± 0.039	0.070 ± 0.045
(Max Like)	(0.95)	(1.31)	(2.40)	(0.86)	(1.36)	(25.9)	(5.1)	(0.106)	(0.137)

Note. — Best values and error estimates (see §6.4.1) for the fundamental free parameters of the fiducial HE model. $P_{\rm ref}$ refers to the total gas pressure evaluated at the reference radius r = 10 kpc and serves as the boundary condition for the hydrostatic model. The parameters s_0, s_1, and α_1 specify the power-law plus constant entropy profile. The fundamental mass parameters are the H-band stellar mass-to-light ratio ($M_\star/L_H$), and the concentration and enclosed total mass (stars+gas+DM) computed within r_{200}. Note the gas and baryon fractions are parameters derived from the mass model.

over, fits using the NFW and Einasto profiles are indistinguishable and yield similar parameter values. These results are fully consistent with what we found for NGC 6482 (B17).

6.4.4. *SMBH*

While we fixed the SMBH mass by default in our models, we found that the *Chandra* data were able to constrain $M_{\rm BH}$, albeit weakly. The key reason why only weak constraints are possible with the present data is that the central aperture has a radius 1.″7 whereas the SMBH radius of influence is $r_g \approx 0.''5$. Using a flat prior for $M_{\rm BH}$ over the range $(0.3-20)\times10^9 M_\odot$ we obtain $M_{\rm BH} = (5\pm4)\times10^9 M_\odot$, with a 90% upper limit of $M_{\rm BH} = 1.4\times10^{10} M_\odot$, very consistent with the recent stellar dynamical measurement by Walsh et al. (2017).

If instead we use a flat prior on the logarithm, the SMBH is not detected and a more stringent upper limit is indicated: $M_{\rm BH} = (1.4\pm1.7)\times10^9 M_\odot$, with a 99% upper limit of $M_{\rm BH} = 9.4\times10^9 M_\odot$. The sensitivity of $M_{\rm BH}$ to the prior shows that the parameter is not constrained robustly by our bayesian analysis. A standard frequentist χ^2 fit yields $M_{\rm BH} = (3.9\pm2.6)\times10^9 M_\odot$ more in line with the result for the flat (non-logarithm) prior. We conclude that the present data are consistent with the $M_{\rm BH}$ determination by Walsh et al. (2017), and improvement in the constraint awaits precise measurements of the hot ISM properties in a smaller aperture closer to r_g.

We note that omitting the SMBH from the HE models has a negligible impact on the quality of the fit. Consequently, the centrally peaked temperature profile (Figure 5) is not caused by the gravitational influence of the SMBH, nor is it due to hard emission from an AGN (§6.2). The centrally peaked temperature profiles observed in several massive elliptical galaxies (e.g., NGC 6482, B17) may be explained by classical wind models (e.g., David et al. 1991; Ciotti et al. 1991).

6.4.5. *Stellar Mass and IMF*

The result we obtain for the stellar mass-to-light ratio, $M_\star/L_H = 1.33\pm0.21$ solar, agrees very well with the stellar-dynamical analysis of Walsh et al. (2017) who found $M_\star/L_H = 1.3\pm0.4$ solar. Walsh et al. (2017) report their value also agrees with that of Y17 and is consistent with single-burst stellar population synthesis models with either a Kroupa ($M_\star/L_H$ = 1.2 solar) or Salpeter ($M_\star/L_H$ = 1.7 solar) IMF. However, the smaller error bar we obtain for $M_\star/L_H$ remains fully consistent with the Kroupa IMF but is marginally inconsistent ($\approx 2\sigma$) with the Salpeter IMF.

The agreement with a Kroupa (or Chabrier) IMF we find for Mrk 1216 is typical for X-ray HE studies of massive elliptical galaxies (see discussion in §8.3 of B17). We also note that our result for Mrk 1216 is not dependent on our use of the accurate MGE model of the H-band light (§6.3). If instead we use a de Vaucouleurs model with the half-light radius from the Two Micron All-Sky Survey (2MASS) Extended Source Catalog (Jarrett et al. 2000), we obtain $M_\star/L_H = 1.24\pm0.19$ solar, very consistent with the MGE result.

Finally, we note that the good agreement of the values of $M_\star/L_H$ obtained by us and Walsh et al. (2017) supports the accuracy of the mass-measurement techniques used by both studies; i.e., in our case, the accuracy of the hydrostatic equilibrium approximation for Mrk 1216. Note also that the consistency of the stellar mass supports the stellar mass-size relation for CEGs obtained by Y17 indicating that the structure of the CEGs matches the redshift ~ 2 red nugget population rather than the low-redshift ETG population.

Table 5
Mass-Weighted Total Density Slope and DM Fraction

Radius (kpc)	Radius (R_e)	$\langle\gamma\rangle$	$f_{\rm DM}$
2.3	1.0	2.22 ± 0.08	0.20 ± 0.07
4.6	2.0	2.07 ± 0.09	0.38 ± 0.09
9.2	4.0	1.90 ± 0.07	0.60 ± 0.07
23.0	10.0	1.87 ± 0.13	0.82 ± 0.03

Note. — The mass-weighted slope is evaluated for the fiducial HE model using equation (2) of Dutton & Treu (2014). The DM fraction is defined at each radius r as, $f_{\rm DM} = M_{\rm DM}(<r)/M_{\rm total}(<r)$.

6.4.6. *Density Slope and DM Fraction*

Y17 report an average total mass density slope $\langle\gamma\rangle = 2.3$ within $r = R_e$ for their sample of 16 CEGs. This modestly exceeds the average slopes of normal massive local ETGs (2.15 ± 0.03, intrinsic scatter 0.10) obtained by Cappellari et al. (2015) also within R_e. In Table 5 we list mass-weighted slopes evaluated for several radii. We obtain $\langle\gamma\rangle = 2.22\pm0.08$ within $r = R_e$, which agrees very well with the average CEG value from Y17 and is also consistent with the local ETGs.

Both the average slope we obtain for Mrk 1216 within R_e and its variation with radius broadly agree with the average results of Y17 for CEGs. The CEGs reported by Y17 have average slopes that decrease with radius from a value of 2.3 within $1R_e$ to 1.99 at larger radius. As seen in Table 5, $\langle\gamma\rangle$ for Mrk 1216 decreases with increasing radius out to $10R_e$ and (not shown) begins to increase soon after. For comparison, the instantaneous slope (i.e., not mass-weighted) is ≈ 2.3 near the center, reaches a minimum value of ≈ 1.7 at $r \approx 3R_e$ and

increases for larger radii approaching the slope of 3 for the NFW profile. Cappellari et al. (2015) find an average slope of 2.19 ± 0.03 with 0.11 scatter over $0.1R_e - 4R_e$ for normal ETGs which is significantly larger than the mass-weighted slope we measure within $4R_e$ (1.90 ± 0.07). Hence, like the CEGs studied by Y17, we obtain for Mrk 1216 smaller density slopes than the normal ETGs for radii larger than R_e out to $\approx 4R_e$. (We note that the slope of NGC 6482 (B17) is consistent with the normal ETGs.)

Turning to the DM fraction, Y17 obtain $f_{\rm DM} = 0.11$ within $r = R_e$ for the CEGs which is lower than the value 0.19 of the normal ETGs studied by Cappellari et al. (2015) and accounting for the higher mass range of the CEGs (see Y17). We obtain $f_{\rm DM} = 0.20 \pm 0.07$ (Table 5) for Mrk 1216 which agrees very well with the normal ETGs and is nearly double the value of the CEGs, though the difference is only weakly significant.

Finally, the slope-R_e relation (Humphrey & Buote 2010; see also Auger et al. 2010),

$$\gamma = 2.31 - 0.54 \log(R_e/{\rm kpc})$$

predicts an average slope 2.11 for Mrk 1216 over 0.2-10 R_e. The mass-weighted slope we obtain (Table 5) is $\approx 11\%$ below the predicted value but within the observed scatter (Auger et al. 2010); note B17 found NGC 6482 had a slope $\approx 12\%$ above the predicted value.

6.4.7. *Halo Concentration and Mass*

Whereas Y17 and Walsh et al. (2017) were unable to constrain the DM halo concentration using stellar dynamics, we obtain interesting constraints, $c_{200} = 17.5 \pm 6.7$ and $M_{200} = (9.6 \pm 3.7) \times 10^{12} M_\odot$ (Table 4), despite the short *Chandra* exposure. These best-fitting values exceed the value $c_{200} = 6.6$ of the mean $c_{200} - M_{200}$ relation from ΛCDM by $\approx 4\sigma$ (Dutton & Macciò 2014). While the discrepancy is only $\sim 2\sigma$ significant in terms of the measurement error, the large c_{200} may provide evidence for weak adiabatic contraction as we argued for NGC 6482; i.e., the "forced quenching" model of Dutton et al. (2015) implemented as the AC4 model in B17 yields a similar M_{200} and a smaller $c_{200} = 15$ that is less discrepant ($\approx 3\sigma$) with the mean ΛCDM relation (and does not alter the best-fitting $M_\star/L_H$.)

In fact, the concentration discrepancy may be even larger for Mrk 1216. Unlike the results quoted previously for other model parameters (e.g., $M_\star/L_H$) , we find that the concentration values differ by $> 1\sigma$ error depending on how we define the Bayesian best-fitting value. Above we have focused on the "Best Fit" values (see §6.4.1). For well-constrained parameters, the "Best Fit" and "Max Like" parameter values closely correspond; e.g., see the results for NGC 6482 (B17) and RXJ 1159+5531 (Buote et al. 2016). But the concentration and virial mass, which are global halo parameters, are not very well constrained for Mrk 1216 since the *Chandra* measurements of gas temperature and density currently extend only out to an average binned radius $\approx r_{2500}/3$.

The Max Like values we obtain are, $c_{200} = 25.9$ and $M_{200} = 5.1 \times 10^{12} M_\odot$, where c_{200} is over 5σ above the mean ΛCDM relation, almost as discrepant as NGC 6482 (B17). We note also that the Max Like parameters closely correspond to those obtained from a standard frequentist χ^2 fit; i.e., $c_{200} = 25.5$ and $M_{200} = 5.4 \times 10^{12} M_\odot$.

6.4.8. *Gas and Baryon Fraction*

Results qualitatively similar to the concentration are obtained for the global baryon fraction ($f_{\rm b,200}$). While the mean Best Fit value ($f_{\rm b,200} = 0.070 \pm 0.045$) is less than half (and $\approx 2\sigma$ below) the cosmic value (0.155), the Max Like value (0.14) is fully consistent with it. Which of these two values of the baryon fraction better approximates reality is important when considering the "Missing Baryons Problem" at low redshift (Fukugita et al. 1998). If the higher value prevails it would lend support to the notion that, at least in massive elliptical galaxy / small group halos, most of the baryons could be located in the outer halo as part of the hot component – consistent with our results obtained previously for NGC 720, NGC 1521, and NGC 6482 (Humphrey et al. 2011, 2012b; Buote 2017);

Note that we do not estimate the contribution to $f_{\rm b,200}$ from smaller, non-central galaxies as we have done in previous studies since their contribution is expected to be negligible compared to the large statistical errors obtained already for $f_{\rm b,200}$.

6.5. *Error Budget*

We have considered an extensive number of systematic tests and examined their impact on the measured parameters of the HE model. Some of these have been discussed in previous sections; e.g., adding a break radius to the entropy profile (§6.4.2), using a de Vaucouleurs profile of the stellar light (§6.4.5). We considered most of the systematic tests discussed in §7 of B17. However, due to the relatively large statistical errors on the HE parameters for Mrk 1216, we find all of those systematic errors to be negligible in that they are less than the 1σ statistical errors. Consequently, in this section we only summarize a few notable tests associated with choices in the spectral analysis (§4 and §6.2) and the treatment of the plasma emissivity in the HE models (§6.3). All of these tests had no significant effect on the HE parameters.

Constant Metallicity: Whereas the results we have presented allow the metallicity to vary with radius, we also considered the constant metallicity solution reported in §6.2.

Soft CXB: We examined adjusting the fluxes of the soft CXB components by factors of 0.5 and 2.

Unresolved LMXBs: We examined adjusting the nominal flux of the unresolved LMXB component by factors of 0.5 and 2.

Plasma Emissivity: The plasma emissivity $\Lambda_\nu(T,Z)$ in our fiducial HE model is evaluated self-consistently at any radius using the temperature of the model. The metallicity used to evaluate $\Lambda_\nu(T,Z)$ at any radius is obtained by fitting a projected, emission-weighted smooth model to the measured metallicity profile (Table 3). The smooth model we use is essentially a β model plus a constant. For comparison, we also adopted the procedure we have favored in our previous studies (e.g., see §4 of B17) of interpolating the radial grid established by the measured binned metallicities in projection as a proxy for the three-dimensional metallicity profile.

7. DISCUSSION AND CONCLUSIONS

We have found for Mrk 1216 that the entropy profile and global mass properties (c_{200}, M_{200}) are very similar to those of the fossil group NGC 6482 (B17) and the massive, isolated nearly fossil[4] systems NGC 720 (Humphrey et al. 2011)

[4] Although NGC 720 and NGC 1521 are typically classified as members of larger groups owing to more distant galaxy associations, we refer to them

and NGC 1521 (Humphrey et al. 2012b). Although for PGC 032873 the *Chandra* data did not allow for detailed HE analysis, we can place its X-ray properties in context, along with those of Mrk 1216, through comparison with global X-ray scaling relations.

The ETG scaling relations for local galaxies seriously underpredict the X-ray luminosities we have measured for Mrk 1216 and PGC 032873. The $L_{\rm x}-T_{\rm x}$ relation reported by Goulding et al. (2016) for the most massive nearby ellipticals predicts $L_{\rm x}\approx 7\times10^{40}$ erg s^{-1} in the 0.3-5.0 keV band for Mrk 1216 while we measure a value $\sim 1\times10^{42}$ erg s^{-1} in the same band that is a factor of ~ 14 times larger. For PGC 032873 the difference is a factor of ~ 3. The $L_{\rm x}, L_{\rm K}, \sigma_e$ scaling relation of Goulding et al. (2016) yields even larger factors[5]. The fact that Mrk 1216 and PGC 032873 have $L_{\rm x}$ values that greatly exceed the scaling relations of normal ETGs is unsurprising since the total masses inferred for these galaxies ($\sim 10^{13} M_\odot$) indicate group-scale halos (even though both galaxies are rather isolated – e.g., Ferré-Mateu et al. 2017). Indeed, using the $L_{\rm x}-T_{\rm x}$ results for galaxy groups by Lovisari et al. (2015) with the average temperatures we have measured (Table 1) yields good agreement for Mrk 1216 but overpredicts $L_{\rm x}$ for PGC 032873 by a factor of ~ 5; i.e., PGC 032873 lies roughly midway between the scaling relations for ETGs and groups.

If these CEGs are indeed largely untouched descendents from the $z\sim 2$ population of red nuggets (Ferré-Mateu et al. 2017; Y17) that undergo little "phase 2" stellar accretion over that time, it is remarkable that they are each the dominant central galaxy in a group-size halo. Apparently all the merging in these groups occurred in the assembly of the red nugget, making these systems truly ancient fossil groups.

The results we have presented in this paper were first summarized in observing proposals submitted to the *Chandra* AO19 and *XMM-Newton* AO17 calls for proposals in 2017. Both proposals were approved for deep follow-up observations of Mrk 1216.

We thank the anonymous referee and Dr. A. Yıldırım for comments on the manuscript. DAB gratefully acknowledges partial support from the National Aeronautics and Space Administration (NASA) under Grant NNX15AM97G issued through the Astrophysics Data Analysis Program. This research has made use of the NASA/IPAC Extragalactic Database (NED) which is operated by the Jet Propulsion Laboratory, California Institute of Technology, under contract with the National Aeronautics and Space Administration.

REFERENCES

Arnaud, K. A. 1996, in Astronomical Society of the Pacific Conference Series, Vol. 101, Astronomical Data Analysis Software and Systems V, ed. G. H. Jacoby & J. Barnes, 17
Asplund, M., Grevesse, N., & Jacques Sauval, A. 2006, Nuclear Physics A, 777, 1
Auger, M. W., Treu, T., Bolton, A. S., et al. 2010, ApJ, 724, 511
Blumenthal, G. R., Faber, S. M., Flores, R., & Primack, J. R. 1986, ApJ, 301, 27
Buote, D. A. 2000a, ApJ, 539, 172
—. 2000b, MNRAS, 311, 176
—. 2017, ApJ, 834, 164
Buote, D. A., & Canizares, C. R. 1994, ApJ, 427, 86
Buote, D. A., & Humphrey, P. J. 2012a, in Astrophysics and Space Science Library, Vol. 378, Astrophysics and Space Science Library, ed. D.-W. Kim & S. Pellegrini, 235
Buote, D. A., & Humphrey, P. J. 2012b, MNRAS, 421, 1399
Buote, D. A., Lewis, A. D., Brighenti, F., & Mathews, W. G. 2003, ApJ, 595, 151
Buote, D. A., Su, Y., Gastaldello, F., & Brighenti, F. 2016, ApJ, 826, 146
Cappellari, M., Romanowsky, A. J., Brodie, J. P., et al. 2015, ApJ, 804, L21
Carter, D., & Metcalfe, N. 1980, MNRAS, 191, 325
Cash, W. 1979, ApJ, 228, 939
Cavaliere, A., & Fusco-Femiano, R. 1978, A&A, 70, 677
Ciotti, L., D'Ercole, A., Pellegrini, S., & Renzini, A. 1991, ApJ, 376, 380
Condon, J. J., Cotton, W. D., Greisen, E. W., et al. 1998, AJ, 115, 1693
David, L. P., Forman, W., & Jones, C. 1991, ApJ, 369, 121
Dutton, A. A., & Macciò, A. V. 2014, MNRAS, 441, 3359
Dutton, A. A., Macciò, A. V., Stinson, G. S., et al. 2015, MNRAS, 453, 2447
Dutton, A. A., & Treu, T. 2014, MNRAS, 438, 3594
Feroz, F., Hobson, M. P., & Bridges, M. 2009, MNRAS, 398, 1601
Ferré-Mateu, A., Mezcua, M., Trujillo, I., Balcells, M., & van den Bosch, R. C. E. 2015, ApJ, 808, 79
Ferré-Mateu, A., Trujillo, I., Martín-Navarro, I., et al. 2017, MNRAS, 467, 1929
Fujimoto, R., Mitsuda, K., Mccammon, D., et al. 2007, PASJ, 59, 133
Fukugita, M., Hogan, C. J., & Peebles, P. J. E. 1998, ApJ, 503, 518
Gnedin, O. Y., Kravtsov, A. V., Klypin, A. A., & Nagai, D. 2004, ApJ, 616, 16
Goulding, A. D., Greene, J. E., Ma, C.-P., et al. 2016, ApJ, 826, 167
Huang, S., Ho, L. C., Peng, C. Y., Li, Z.-Y., & Barth, A. J. 2013, ApJ, 768, L28
Humphrey, P. J., & Buote, D. A. 2006, ApJ, 639, 136
—. 2008, ApJ, 689, 983
—. 2010, MNRAS, 403, 2143
Humphrey, P. J., Buote, D. A., Brighenti, F., et al. 2012a, ApJ, 748, 11
Humphrey, P. J., Buote, D. A., Brighenti, F., Gebhardt, K., & Mathews, W. G. 2008, ApJ, 683, 161
—. 2009a, ApJ, 703, 1257
Humphrey, P. J., Buote, D. A., Canizares, C. R., Fabian, A. C., & Miller, J. M. 2011, ApJ, 729, 53
Humphrey, P. J., Buote, D. A., Gastaldello, F., et al. 2006, ApJ, 646, 899
Humphrey, P. J., Buote, D. A., O'Sullivan, E., & Ponman, T. J. 2012b, ApJ, 755, 166
Humphrey, P. J., Liu, W., & Buote, D. A. 2009b, ApJ, 693, 822
Irwin, J. A., Athey, A. E., & Bregman, J. N. 2003, ApJ, 587, 356
Jarrett, T. H., Chester, T., Cutri, R., et al. 2000, AJ, 119, 2498
Kalberla, P. M. W., Burton, W. B., Hartmann, D., et al. 2005, A&A, 440, 775
Lovisari, L., Reiprich, T. H., & Schellenberger, G. 2015, A&A, 573, A118
Matsumoto, H., Koyama, K., Awaki, H., et al. 1997, ApJ, 482, 133
McConnell, N. J., Ma, C.-P., Murphy, J. D., et al. 2012, ApJ, 756, 179
Mernier, F., de Plaa, J., Kaastra, J. S., et al. 2017, A&A, 603, A80
Navarro, J. F., Frenk, C. S., & White, S. D. M. 1997, ApJ, 490, 493
Oser, L., Ostriker, J. P., Naab, T., Johansson, P. H., & Burkert, A. 2010, ApJ, 725, 2312
Pratt, G. W., Arnaud, M., Piffaretti, R., et al. 2010, A&A, 511, A85
Rusli, S. P., Thomas, J., Saglia, R. P., et al. 2013, AJ, 146, 45
Thomas, J., Ma, C.-P., McConnell, N. J., et al. 2016, Nature, 532, 340
Tozzi, P., & Norman, C. 2001, ApJ, 546, 63
van den Bosch, R. C. E., Gebhardt, K., Gültekin, K., Yıldırım, A., & Walsh, J. L. 2015, ApJS, 218, 10
van Dokkum, P. G., Franx, M., Kriek, M., et al. 2008, ApJ, 677, L5
Voit, G. M., Kay, S. T., & Bryan, G. L. 2005, MNRAS, 364, 909
Walsh, J. L., van den Bosch, R. C. E., Gebhardt, K., et al. 2015, ApJ, 808, 183
—. 2017, ApJ, 835, 208
Walton, D. J., Roberts, T. P., Mateos, S., & Heard, V. 2011, MNRAS, 416, 1844
Werner, N., Lakhchaura, K., Canning, R. E. A., Gaspari, M., & Simionescu, A. 2017, ArXiv e-prints, arXiv:1711.09983
Werner, N., Urban, O., Simionescu, A., & Allen, S. W. 2013, Nature, 502, 656
Yıldırım, A., van den Bosch, R. C. E., van de Ven, G., et al. 2017, MNRAS, 468, 4216
—. 2016, MNRAS, 456, 538

as "nearly" fossil systems since they obey the fossil classification within their projected virial radii.

[5] In these comparisons we have used the "full aperture" scaling relations of Goulding et al. (2016) defined within the radius where the diffuse hot gas flux equals the background. For Mrk 1216 this corresponds to Annulus 7 and leads to an $L_{\rm x}\approx 0.95\%$ of the value at 100 kpc listed in Table 1. For PGC 032873 the corresponding radius is $\approx 0\farcm3$ and $L_{\rm x}\approx 0.6$ of the value at 100 kpc.